FULL PAPER

ADVANCED
ENERGY
MATERIALS

www.advenergymat.d

Check for updates

Ultrathin Nanosheets of Oxo-functionalized Graphene Inhibit the Ion Migration in Perovskite Solar Cells

Meng Li, Wei-Wei Zuo, Qiong Wang, Kai-Li Wang, Ming-Peng Zhuo, Hans Köbler, Christian E. Halbig, Siegfried Eigler,* Ying-Guo Yang, Xing-Yu Gao, Zhao-Kui Wang,* Yongfang Li, and Antonio Abate*

Mixed cation/halide perovskites have led to a significant increase in the efficiency and stability of perovskite solar cells. However, mobile ionic defects inevitably exacerbate the photoinduced phase segregation and self-decomposition of the crystal structure. Herein, ultrathin 2D nanosheets of oxo-functionalized graphene/dodecylamine (oxo-G/DA) are used to solve ion migration in cesium (Cs)-formamidinium (FA)-methylammonium (MA) triple-cation-based perovskites. Based on the superconducting carbon skeleton and functional groups that provide lone pairs of electrons on it, the ultrathin 2D network structure can fit tightly on the crystals and wrap them, isolating them, and thus reducing the migration of ions within the built-in electric field of the perovskite film. As evidence of the formation of sharp crystals with different orientation within the perovskite film, moiré fringes are observed in transmission electron microscopy. Thus, a champion device with a power conversion efficiency (PCE) of 21.1% (the efficiency distribution is 18.8 ± 1.7%) and a remarkable fill factor of 81%, with reduced hysteresis and improved long-term stability, is reported. This work provides a simple method for the improvement of the structural stability of perovskite in solar cells.

1. Introduction

Organic–inorganic hybrid perovskite solar cells (PSCs) have attracted enormous interest with rapid progress in power conversion efficiency (PCE) from 3.8% to the present record of 25.2%.[1–8] Recent progress of PSCs in efficiency and stability enhancement is addressed to the change of perovskite composition and crystal optimization. By introducing mixed cations and halide to adjust the composition of the organic–inorganic hybrid perovskite, the crystal structure of the perovskite can be effectively improved, which ultimately led to the increased stability and efficiency of the PSCs. Compared with the single cation/halide perovskite (methylammonium halide, formamidinium lead halide, and cesium lead halide), the mixed perovskite not only has higher PCE but also has better heat and humid air stability.[9–12]

For mixed cation/halide perovskites, despite good optoelectronic properties, the mixing of multiple cations and halogens is prone to localized ionic enrichment during preparation, annealing, and operation. At the same time, as the cation and halide ions move in the built-in electric field of the device, local positive and negative ion vacancies are formed. These defects will cause significant hysteresis in the device and ultimately affect the performance of the device.[13–17] A series of studies on both experimental and theoretical methods[13,18,19] have been reported. Constraining

Dr. M. Li, K.-L. Wang, M.-P. Zhuo, Prof. Z.-K. Wang
Institute of Functional Nano & Soft Materials (FUNSOM)
Jiangsu Key Laboratory for Carbon-Based Functional Materials & Devices
Soochow University
Suzhou 215123, China
E-mail: zkwang@suda.edu.cn

Dr. M. Li, W.-W. Zuo, Dr. Q. Wang, H. Köbler, Prof. A. Abate
Helmholtz-Zentrum Berlin für Materialien und Energie
Kekuléstraße 5, 12489 Berlin, Germany
E-mail: antonio.abate@helmholtz-berlin.de, antonio.abate@unina.it

The ORCID identification number(s) for the author(s) of this article can be found under https://doi.org/10.1002/aenm.201902653.

Dr. M. Li, Prof. Y. F. Li
Laboratory of Advanced Optoelectronic Materials
College of Chemistry
Chemical Engineering and Materials Science
Soochow University
Suzhou 215123, China

Dr. C. E. Halbig, Prof. S. Eigler
Institute of Chemistry and Biochemistry
Takustraße 3, 14195 Berlin, Germany
E-mail: siegfried.eigler@fu-berlin.de

Dr. Y.-G. Yang, Prof. X.-Y. Gao
Shanghai Synchrotron Radiation Facility(SSRF)
Zhangjiang Lab.
Shanghai Advanced Research Institute
Chinese Academy of Sciences
239 Zhangheng Road, Shanghai 201204, China

Prof. A. Abate
Department of Chemical, Materials and Production Engineering
University of Naples Federico II
Piazzale Tecchio 80, Fuorigrotta 80125, Naples, Italy

ADVANCED
SCIENCE NEWS
www.advancedsciencenews.com

ADVANCED
ENERGY
MATERIALS
www.advenergymat.de

the pathways of the ionic migration and inhibiting mobile ions are straightforward and effective ways to inhibit the ion migration in perovskites. In this regard, ion migration inhibition can be achieved by passivating the grain boundary, regulating the crystal growth process or using additives to inhibit the movement of ions themselves.[20–22]

Oxo-functionalized graphene (oxoG) and its reduced analogue are a novel 2D network structure materials with excellent electrical conductivity, desirable semiconducting properties, and superior chemical stability, which has been successfully utilized in the field of the solar cell, and memory devices.[23–27] Herein, we report on ultrathin 2D nanosheets of oxo-functionalized graphene/dodecylamine (oxo-G/DA) incorporated into triple cation PSCs by solution processing, leading to high efficiency and durability.[23–25] The use of DA-modified oxo-G not only increases the dispersibility of oxo-G/DA in an organic solvent, which even forms a large number of single-layer nanosheets under its action. At the same time, lone pair electrons supported by C—O and π-electrons in the superconducting carbon skeleton which can form σ-bond between oxo-G/DA and cations during the crystallization process, the lone pair of electrons provided by oxo-G/DA can form a sigma coordinate bond with the cation in the perovskite precursor solution, so that oxo-G/DA can be attached and encapsulated in perovskite crystals after annealing. And the amino chain can also optimize the interface with crystal grains in perovskite layers, reducing defects at grain boundaries. With the introduction of oxo-G/DA into perovskite, the crystallization of perovskites has been improved, and the grain size has nearly doubled. Improvements in film crystal properties and optoelectronic properties are more conducive to charge generation, separation and transmission. Simultaneously, the ultrathin 2D network structure nanosheets well block the oxygen and moisture in the environment, which makes the stability of the device significantly improved. The

champion solar cell with oxo-G/DA exhibits significant increase of PCE from 19.0 (16.5 ± 1.3%) to 21.1% (18.8 ± 1.7%), and with an open-circuit voltage (V_{oc}) of 1.13 V, a short-circuit current density (J_{sc}) of 23.1 mA cm^{-2}, and a fill factor (FF) of 81%. The stability of PSCs with oxo-G/DA maintains 70% of the initial PCE after 960 h without any encapsulation under room temperature.

2. Results and Discussion

2.1. The Operational Mechanism of Oxo-G/DA

In order to well understand the effect of ultrathin 2D nanosheets of oxo-G/DA on the performance of perovskite solar cells, we prepared $Cs_{0.05}(FA_{0.85}MA_{0.15})_{0.95}Pb(I_{0.85}Br_{0.15})_3$ triple-cation-based PSCs by incorporating oxo-G/DA to the precursor solution (Figure S1, Supporting Information) and the n–i–p planar perovskite solar cells were fabricated with a structure of fluorine-doped tin oxide (FTO)/SnO$_x$/(perovskite:oxo-G/DA)/Spiro-OMeTAD/Au, as shown in **Figure 1**a. Figure 1b shows the chemical structure of oxo-G/DA. It can be seen that, unlike conventional graphene and other oxygenated/oxidized/oxygen-containing graphene derivatives (e.g., graphene oxide), oxo-G/DA possesses organosulfur groups on the basal plane of graphene and dodeclyamonium groups anchored to those for charge neutralization ($C_{12}H_{25}NH_3^+$). The chemical structure was thoroughly investigated in an earlier study.[25] The amino chain can promote the dispersion of oxo-G in the perovskite precursor and even form a large number of monolayer-distributed structures. In several reports, we have verified the size and layer distribution of oxo-G/DA nanosheets by particle size analyzer and atomic force microscopy (AFM). It can be seen that the diameter of graphene is mainly distributed
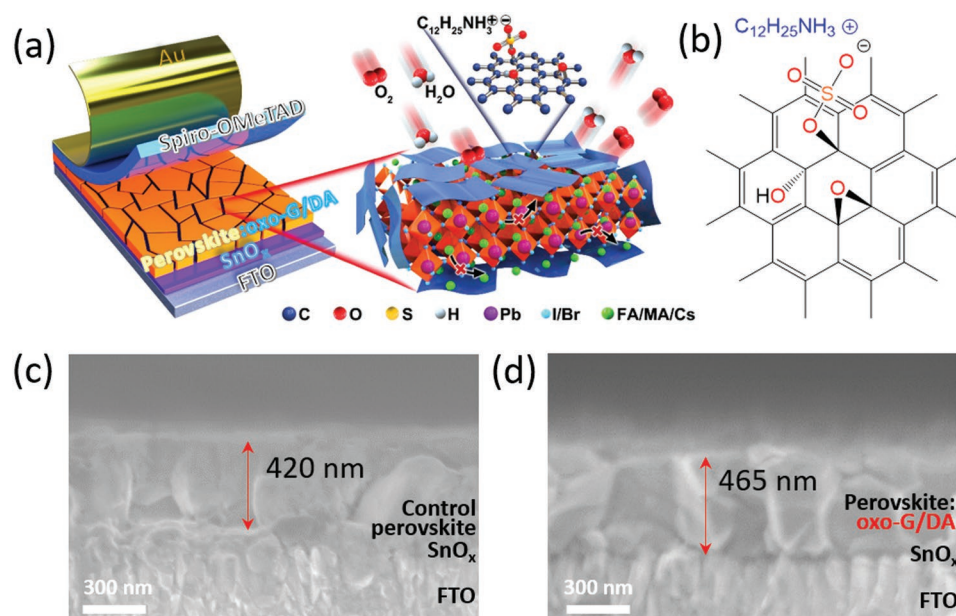
Figure 1. a) Schematic of perovskite solar cell (left) and simulation of the distribution between ultrathin oxo-G/DA nanosheets and perovskite crystals (right); b) simplified chemical structure of oxo-G/DA; cross-sectional SEM image of c) control perovskite and d) perovskite:oxo-G/DA based on FTO/SnO$_x$.
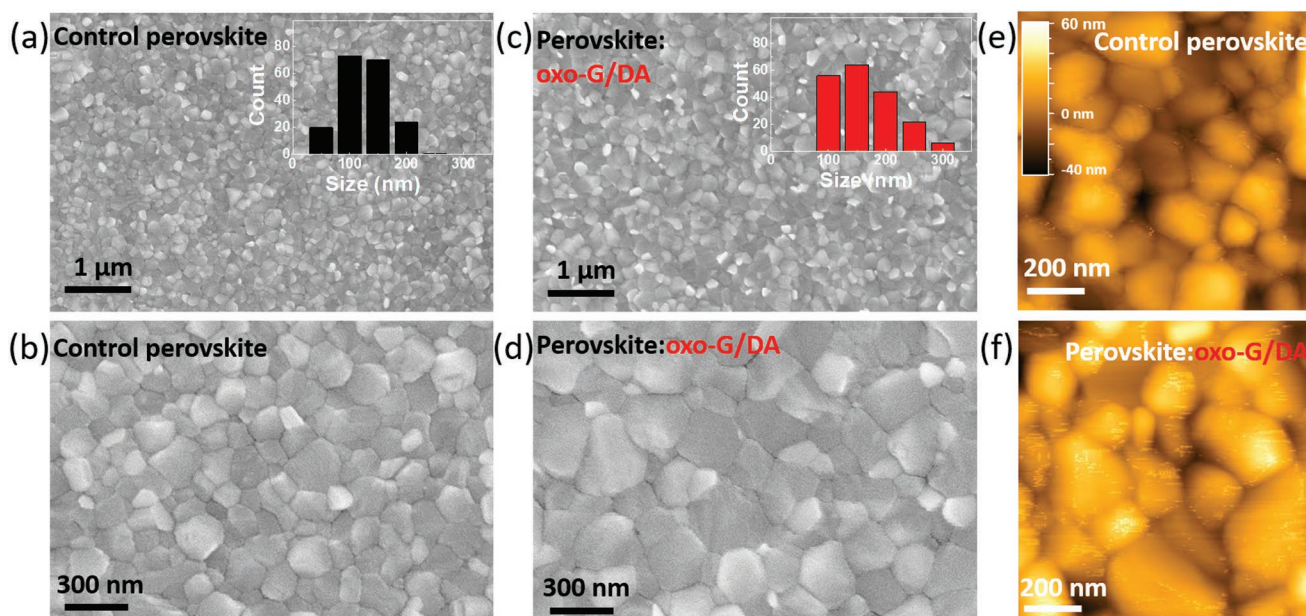
Figure 2. SEM images of a,b) control perovskite and c,d) perovskite:oxo-G/DA films deposited on FTO/SnO$_x$ substrates. The insets of (a) and (c) are the statistical diagrams of corresponding grain size distribution. AFM images of e) control perovskite and f) perovskite:oxo-G/DA films.

in the range of 50–800 nm, and the thickness is within 1 nm.[23–25,28] The microstructure of the ultrathin nanosheets of oxo-G/DA-wrapped perovskite formed during the crystallization of perovskite can effectively reduce the defects of oxo-G/DA agglomeration formation. Figure 1c,d shows cross-sectional scanning electron microscope (SEM) images of the perovskite and perovskite:oxo-G/DA films on FTO/SnO$_x$. It can be seen that incorporating oxo-G/DA improves the crystal formation of the perovskite, which makes the grain of the perovskite film larger and also increases the thickness of the perovskite absorber layer. From the optical photograph of the perovskite films (Figure S2, Supporting Information), the oxo-G/DA slows down the crystallization of the perovskite during the annealing process, which makes the corresponding crystal grains larger. This morphological difference is consistent with other reported results of 2D material doped perovskites.[29,30]

2.2. Characterization of Perovskite:Oxo-G/DA Films

For perovskite photovoltaic devices, the effect of the crystallization and film morphology of the light-absorbing layer on the optoelectronic properties is critical. To further investigate the impact of oxo-G/DA on the crystallization of perovskite films, SEM was used to study the surface morphology of perovskite films. **Figure 2**a–d shows the SEM surface morphology images of perovskite films without and with oxo-G/DA nanosheets. The incorporation of oxo-G/DA increases the grain size of the perovskite film. For the control perovskite film (Figure 2a,b), the perovskite has relatively small grains, while for the perovskite:oxo-G/DA films (Figure 2c,d), the grain has a significant increase. The statistical variation in the grain size of the perovskite films (the inset of Figure 2a,b) shows that the average grain size increases from 110 to 195 nm after incorporating

oxo-G/DA into perovskite. AFM was used to study the variation of the roughness of perovskite film. Figure 2e,f shows the AFM images of control perovskite and perovskite:oxo-G/DA films, respectively. The roughness of the perovskite film changed from 9.2 to 13.1 nm after incorporating oxo-G/DA into perovskite, indicating that while the grain size of the film increases, the roughness does not change much for the perovskite:oxo-G/DA films. This trend demonstrates that the roughness of the film does not vary significantly with the increase of the grain size of the film.

For gaining a deeper understanding of the influence of oxo-G/DA on the electronic structure of perovskite crystals, the perovskite films were scraped off, and then the obtained powder was put onto a copper net for microscopic evaluation. **Figure 3**a,b shows the particles of perovskite and perovskite:oxo-G/DA scraped from their corresponding films, and particle sizes are around a few hundred nanometers. Figure 3c,d shows transmission electron microscopy (TEM) images of perovskite and perovskite:oxo-G/DA films. The lattice parameter of $Cs_{0.05}(FA_{0.85}MA_{0.15})_{0.95}Pb(I_{0.85}Br_{0.15})_3$ film was determined to be 0.31 nm, which can be indexed by (220) plane of the tetragonal phase. Similarly, there is almost no change in the lattice for perovskite:oxo-G/DA films.[31–34] This trend indicates the oxo-G/DA does not change the lattice parameters of the perovskite film. However, it can be seen in Figure 3e that in the perovskite:oxo-G/DA sample, moiré fringes appear at grain boundaries between the two crystal grains. This indicates that oxo-G/DA causes changes in the crystal structure of the perovskite grain edge. And moiré fringes are formed by a plurality of perovskite grains with different orientations of crystal lattice planes. A large number of moiré fringes demonstrate lattice relaxation of adjacent perovskite crystals. It is beneficial to improve the order and stability of the interfacial structure of the perovskite crystal.
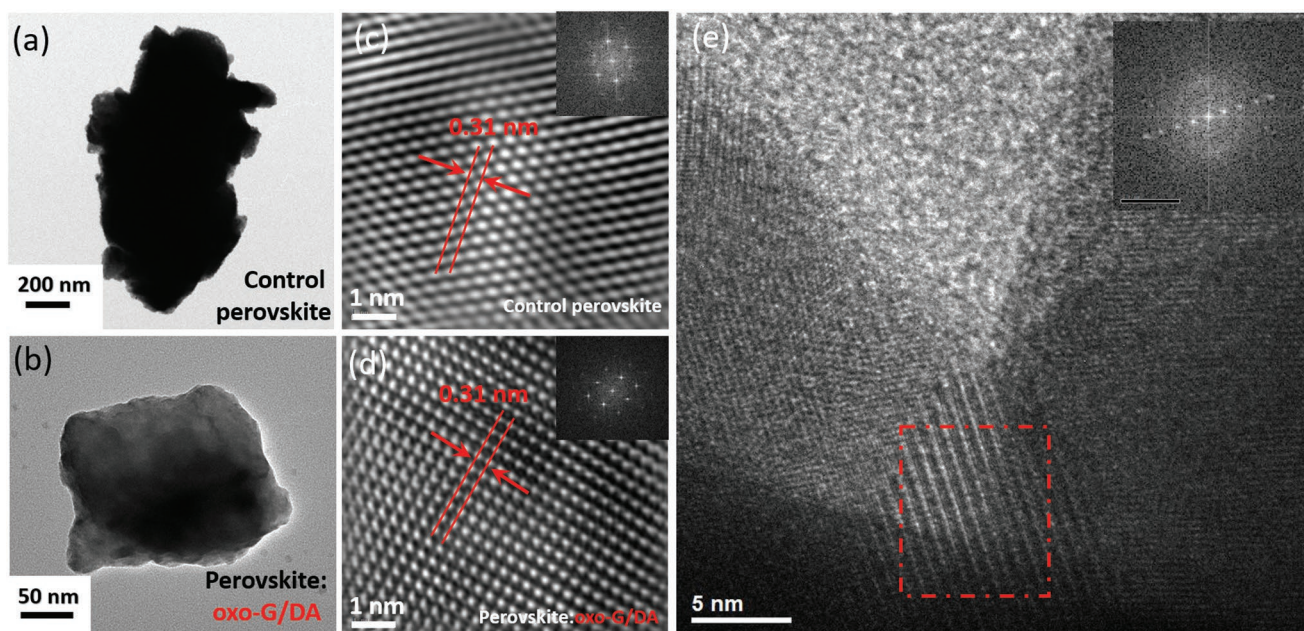
Figure 3. TEM images of a) control perovskite and b) perovskite:oxo-G/DA particles; the atomic resolution TEM images of c) control perovskite and d) perovskite:oxo-G/DA films; insets are Fourier transforms. e) The lattice distribution of the grain boundaries between the two grains for perovskite:oxo-G films; insets are Fourier transforms inside the red square part.

2.3. Photovoltaic Performance of Perovskite:Oxo-G/DA

Figure 4a displays the current density–voltage (J–V) curves of the control perovskite and perovskite:oxo-G/DA (2% vol) PSCs under AM 1.5G illumination with the light intensity of 100 mW cm^{-2}. The device of perovskite:oxo-G/DA (2% vol) PSCs exhibits a highest PCE of 21.1%, an open-circuit voltage (V_{oc}) of 1.13 V, a short-circuit current density (J_{sc}) of 23.1 mA cm^{-2}, and a fill factor (FF) of 81%, while control perovskite devices show a PCE of 19.0%, a V_{oc} of 1.10 V, a J_{sc} of 22.1 mA cm^{-2}, and an
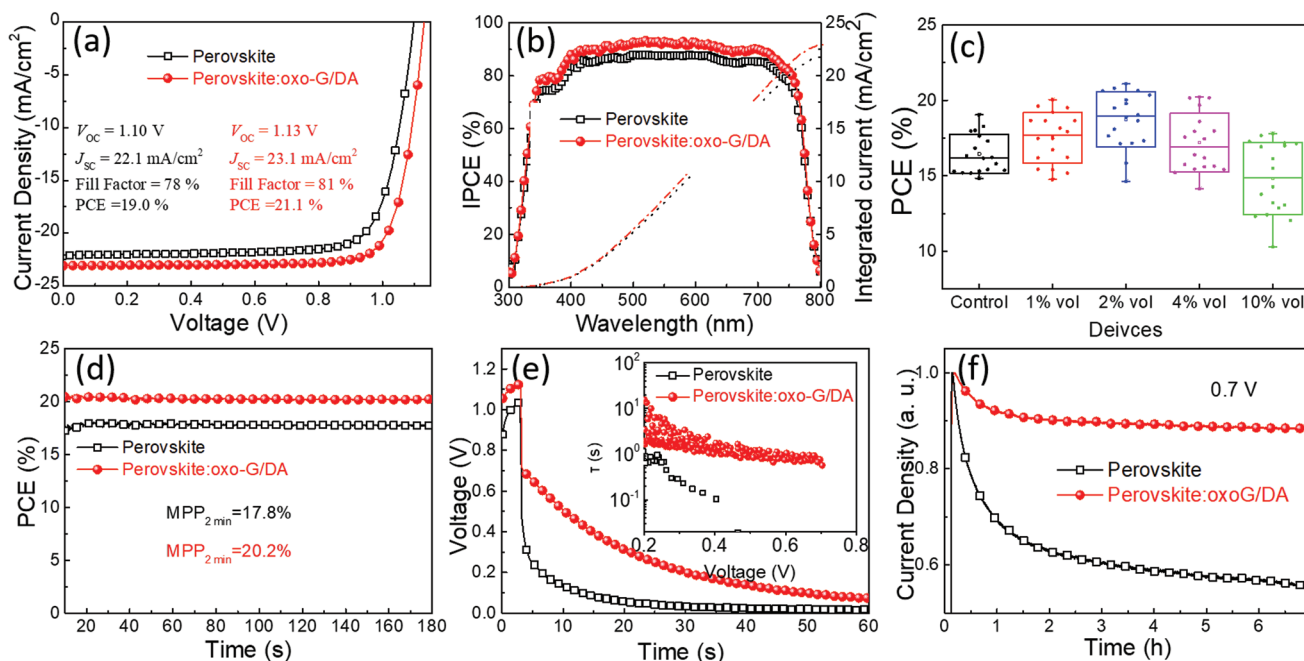
Figure 4. a) J–V curves of the control and doped oxo-G/DA devices under 100 mW cm^{-2}. b) IPCE spectra and c) histogram of PCEs. d) Steady-state efficiency of control and the optimized perovskite-oxo-G/DA solar cells at the maximum power point. e) Open-circuit photovoltage decay (OCVD) curves for the two devices. The inset is the calculated carrier lifetime curve. f) Current transient decay curves for the two devices.

FF of 78%. The J–V curves of devices with different amounts of oxo-G/DA adding into perovskite precursor solution were also measured (Figure S3, Supporting Information). The key cell parameters of V_{oc}, J_{sc}, FF, and PCE are summarized in Table S1 (Supporting Information). It can be seen that the J_{sc}, and V_{oc} of the device increased significantly after adding oxo-G/DA. The increase in J_{sc} is mainly due to the improvement of light absorption within the perovskite film (Figure S4, Supporting Information), which is caused by the improvement of film thickness after adding oxo-G/DA.[30] The improvement in V_{oc} and FF is attributed to the improved grain size and decreased pinholes.[35] The better crystal quality can effectively increase the charge collection and transport in the perovskite film, while the fewer and more optimized grain boundaries also reduce the defects in the film, which is also consistent with the results of other research.[8,36,37]

The incident photon-to-current efficiency (IPCE) spectra for the control and the perovskite:oxo-G/DA devices are displayed in Figure 4b. The integrated current from IPCE and the J_{sc} obtained from the J–V curve are consistent, and the IPCE spectrum of the perovskite:oxo-G/DA device is increased from the wavelength range of 400–700 nm compared to a control device. The reproducibility of PCE, V_{oc}, J_{sc}, and FF for different oxo-G/DA concentrations devices were evaluated, as displayed in Figure 4c and Figure S5 (Supporting Information). Figure 4d shows the steady-state efficiency measured at the maximum power point from over 3 min. The PCE of the perovskite:oxo-G/DA device stabilized at 20.2%, which was close to the value obtained from the J–V measurement.

To further investigate the electron–hole recombination process, the open-circuit photovoltage decay (OCVD) was measured and shown in Figure 4e, where a fast decay of V_{oc} is observed. The electron lifetimes (τ_n) can be extracted from the following equation

$$\tau_n = \frac{-TK_B}{e}\left(\frac{dV_{oc}}{dt}\right)^{-1} \tag{1}$$

where T is the temperature, K_B is the Boltzmann constant, and e is the elementary charge. The result is given as an inset of Figure 4e. It clearly shows that the electron lifetime in the perovskite:oxo-G/DA film is longer than that in the control film, which indicates that the recombination of holes and electrons in the perovskite layer was blocked by oxo-G/DA nanosheets. This also explains the higher V_{oc} obtained for the perovskite:oxo-G/DA based PSCs.[38,39] Besides, steady-state photoluminescence (PL) spectra are also used to identify the charge-transporting process and contact resistance in perovskite:oxo-G/DA planar PSCs (Figure S6, Supporting Information), which indicates the positive role of oxo-G/DA in reducing the emission from radiative recombination and thus improving the electron extraction from the perovskite layer.

To provide evidence that the ion migration of the perovskite after doping oxo-G/DA has been effectively suppressed, the current transient dynamics were measured.[40] During the experiment, the devices were kept under 0.01 Sun-equivalent illumination at a bias of 0.7 V and under an N_2 atmosphere. Control perovskite and perovskite:oxo-G/DA devices were continuously tracked for 7 h. It can be seen that the current density

of the perovskite:oxo-G/DA device is very stable while the current density of the control device has been significantly reduced. This trend indicates that the addition of oxo-G/DA effectively alleviates the movement of cations and halide. Furthermore, the forward and reverse scan of J–V curves revealed that the perovskite:oxo-G/DA devices have a much lower hysteresis, which is originated from both suppressed ion migration and the decrease in defects at the surface of perovskite/charge selective contacts (Figure S7 and Table S2, Supporting Information).

2D grazing incidence X-ray diffraction (GIXRD) was further utilized to study the crystal characteristics of perovskite films.[41,42] Figure 5a,b plots the 2D GIXRD profiles of the perovskite and perovskite:oxo-G/DA films. It can be seen that the (110) diffraction peak of the perovskite:oxo-G/DA is significantly enhanced compared with the control film. This result is also consistent with the results of X-ray diffraction measurement (Figure 5c and Figure S8, Supporting Information).

To further investigate the distribution of oxo-G/DA and halide in perovskite layer, time-of-flight secondary ion mass spectroscopy (TOF-SIMS) was utilized to investigate the ion migration behavior of S^-, Br^-, and I^- in perovskite:oxo-G/DA PSCs. Figure 5d show that S^-, Br^-, and I^- are evenly distributed in the perovskite layer. This also shows that the doping of oxo-G/DA not only distributes itself uniformly (Figure S9, Supporting Information) but also suppresses local enrichment of halogen ions. Figure 5e displays the control perovskite and perovskite:oxo-G/DA based PSCs without any encapsulation in the dark state under room temperature and with a humidity of 20% ± 5%. The PCE of the perovskite:oxo-G/DA based device remained 70% of the initial value even after 960 h storage, which decreased from 21.0% to 14.6%. However, the PCE of the control device was reduced from 19.0% to 6.4%. Therefore, we conclude that the network of oxo-G/DA provides an excellent barrier to water and oxygen in the environment, as well as improved device stability.

3. Conclusion

The Cs-FA-MA triple-cation perovskite ion migration and local ion enrichment are crucial factors affecting the efficiency and stability of perovskite optoelectronic devices. In this work, we have demonstrated a new strategy to passivate the grain boundaries of perovskites, inhibiting the local migration of cations and halide ions by incorporating an ultrathin 2D network nanosheet oxo-G/DA into the perovskite layer. Oxo-G/DA can improve the crystal growth of perovskite and increase the size of crystal grains. It is also possible to improve the crystal structure at the grain boundary and reduce the defects of the film. Accordingly, the PCE is remarkably improved from 19.0% to 21.1%. This work provides a facile method for enhancing the structural stability of the mixed cation/halide perovskite crystal.

4. Experimental Section

Material Preparation: The preparation of oxo-G and oxo-G/DA was performed basing to the literature-described process.[25] After oxidation of 1 g graphite by 2 g of potassium permanganate in concentrated sulfuric acid (97.5%), stepwise dilute of the reaction
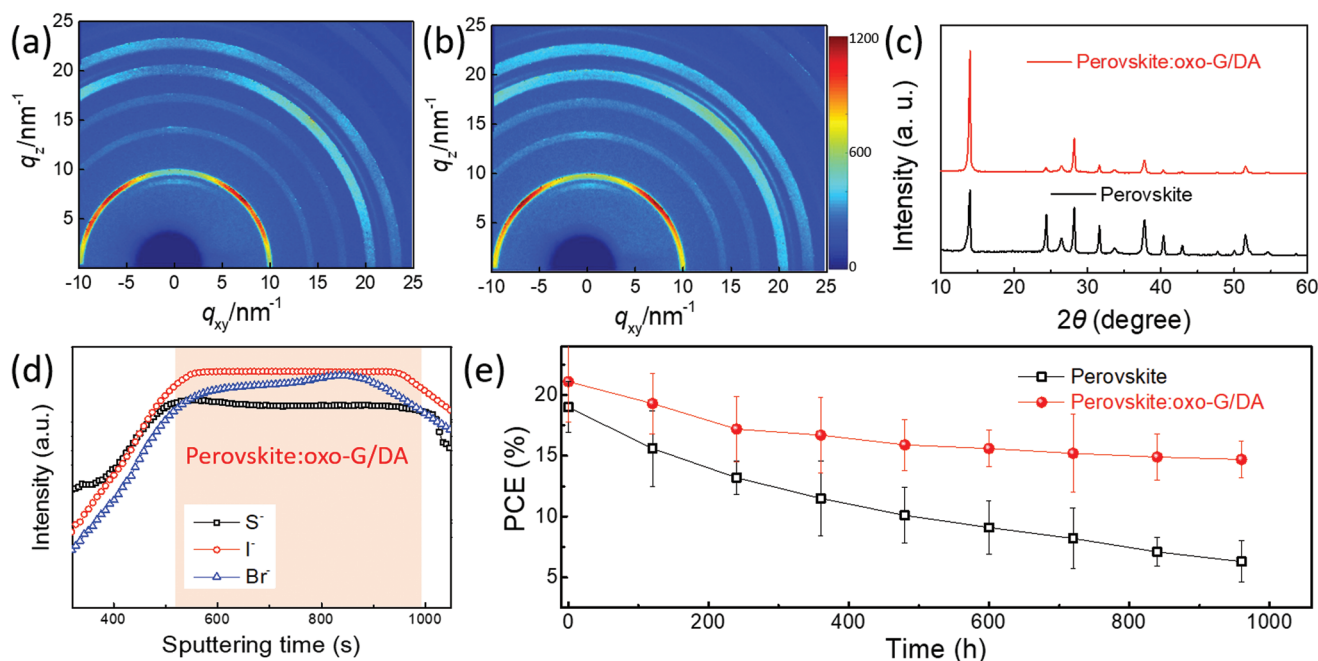
Figure 5. 2D GIXRD patterns of a) control and b) perovskite:oxo-G/DA films. c) XRD spectra of the control and perovskite:oxo-G/DA films. d) TOF-SIMS elemental depth profiles of S⁻, I⁻, and Br⁻ in the control and perovskite:oxo-G/DA-based PSCs. e) Degradation of the PCE values in the control and perovskite:oxo-G/DA-based PSCs as a function of exposure time to air.

mixture and subsequent purification by hydrogen peroxide and repetitive centrifugation, an aqueous dispersion of oxo-G was obtained. The concentration was determined via lyophilization and set to 0.2 mg mL⁻¹.

Elemental Analysis (oxo-G): C = 42.26%, H = 2.81%, N = 0.02%, S = 5.34. The oxo-G stock dispersion was diluted with an equal volume of 2-propanol. Subsequently, hydronium counter ions of organosulfates on oxo-G were exchanged by dropwise addition of a solution of DA (0.1 mg mL⁻¹ in 2-propanol). The ratio of DA to oxo-G was 0.4 mg DA per mg oxo-G. The so formed precipitation was purified by centrifugation for two times using a 1/1 mixture of 2-propanol in water. Finally, the product was dispersed in water and lyophilized.

Device Fabrication: All chemicals without specifications were ordered from Sigma-Aldrich and were used as received without further purification. The device structure was FTO/SnOₓ/perovskite/spiro-OMeTAD/Au. The patterned FTO substrates were cleaned by sonication in soap water, acetone, and ethanol, successively. Following treatment in UV–ozone for 30 min, and then tin oxide were deposited on FTO using chemical bath deposition. 0.02 g tin chloride (SnCl₂*2H₂O) (Sigma-Aldrich), 0.1 g urea (Sigma-Aldrich), 2 μL mercaptoacetic acid (Sigma-Aldrich), and 100 μL hydrochloride acid (HCl, aq 37%) (Sigma-Aldrich) were added into 160 mL ultrapure water. The cleaned FTO was immersed into the above solution and then transferred into an oven at 75 °C for 4 h. Then the substrates were annealed at 180 °C for 1 h and treated under UV–ozone for 15 min. Then the triple cation perovskite, Cs₀.₀₅(FA₀.₈₅MA₀.₁₅)₀.₉₅Pb(I₀.₈₅Br₀.₁₅)₃, was prepared. The solution of CsI (Sigma-Aldrich) in dimethyl sulfoxide (DMSO) was prepared at a molar concentration of 1.5 M. PbI₂ (Tokyo Chemical Industry) and PbBr₂ (Tokyo Chemical Industry) solution of 1.5 M in a mixture solvent of *N,N*-dimethylformamide (DMF) (Sigma-Aldrich) and DMSO (Sigma-Aldrich) at the volume ratio of 4:1 was prepared freshly. Then scaled 0.077 g of MABr (Dyenamo) and 0.223 g of FAI (Dyenamo) to make the mixed cation and mixed halide perovskite precursor. The concentration of the oxo-G/DA solution (used solvent DMF:DMSO = 4:1) is 1 mg mL⁻¹. Then the oxo-G/DA solution is added to the precursor of the perovskite according to the volume ratio. The volume ratios added are 1% vol, 2% vol, 4% vol, 10% vol, respectively. Then chlorobenzene was used as the antisolvent for the spin coating of perovskite. And the perovskite

films were annealed on a hot plate at the temperature of 100 °C for 40 min. For the hole transport layer, 0.05 g of spiro-OMeTAD (Sigma-Aldrich) was dissolved in 1.4 mL chlorobenzene. Then 20 μL of tBP (4-*tert*-butypyridine) (Sigma-Aldrich), 12 μL of LiTFSI (lithium bis(trifluoromethanesulfonyl) imide) (Sigma-Aldrich) solution (520 mg mL⁻¹ in acetonitrile), and 20 μL of FK209 Co(III)TFSI (tris(2-(1H-pyrazol-1-yl)-4-tertbutylpyridine) cobalt(III) tri[bis(trifluoromethane)sulfonimide]) solution (300 mg mL⁻¹ in acetonitrile) (Sigma-Aldrich) were added into the solution. Then spiro-OMeTAD was deposited at the speed of 1800 rpm for 30 s. Then after storing inside a dry air box 24 h, the samples were transferred into the thermal evaporator for the deposition of 80 nm gold (Sigma-Aldrich).

Characterizations: The *J–V* curves of PSCs were measured using a Wavelabs Sinus-70 LED class AAA solar simulator in air. The light intensity was calibrated with a silicon reference cell from Fraunhofer Institute for Solar Energy Systems. *J–V* scans were performed with a Keithley 2400 SMU, controlled by a measurement control program written in LabView. *J–V* curves were measured at a scan rate of 0.1 V s⁻¹, and the time interval was 50 ms. The device active area was 0.18 cm². The IPCE spectra were recorded with an Oriel Instruments QEPVSI-b system integrated with a Newport 300 W xenon arc lamp, controlled by TracQ-Basic software. Monochromatic light was provided by a Newport Cornerstone 260 monochromator and chopped at a frequency of 78 Hz, and conducted to the device surface via optical fibers. The spectrum distribution of IPCE setup was calibrated using a Si reference cell with known spectral response before the measurement. The absorbance of the perovskite films was measured with an UV–vis spectrophotometer (PerkinElmer Lambda 750). SEM images were collected through a field-emission SEM (Quanta 200 FEG, FEI Co.), AFM images were obtained by Veeco Multimode V instrument in the tapping mode. TEM images were obtained by a TEM (FEI company, Tecnai G2 F20, United States). TEM measurement was performed at room temperature at an accelerating voltage of 200 kV. X-ray diffraction (XRD) patterns of the perovskite films were performed by a PANalytical 80 equipment (Empyrean, Cu Ka radiation). The 2D-GIXRD patterns were measured by exposing the samples to a MarCCD located at a distance of ≈223 mm above the samples and a grazing incidence angle

of 0.2° for 20 s. The time-of-flight secondary ion mass spectrometry (Model TOF-SIMS 5, ION-TOF GmbH) was measured with the pulsed primary ions from a Cs^+ (2 keV) liquid-metal ion gun for the sputtering and a Bi+ pulsed primary ion beam for the analysis (30 keV). The steady-state PL spectra were acquired using Horiba Jobin-Yvon LabRAM HR800 under a 480 nm excitation wavelength. The OCVD of devices was also measured through a programmable Keithley 2400 source meter by switching off the external light source. For lyophilization of the prepared oxo-G and oxo-G/DA nanomaterials, a Martin Christ Alpha 1–2 LDplus was used. Elemental analysis was performed on a VARIO EL purchased from Elementar Analysensysteme GmbH.

Supporting Information

Supporting Information is available from the Wiley Online Library or from the author.

Acknowledgements

Conflict of Interest

The authors declare no conflict of interest.

Keywords

[1] A. Kojima, K. Teshima, Y. Shirai, T. Miyasaka, *J. Am. Chem. Soc.* **2009**, *131*, 6050.

[2] M. Kim, G.-H. Kim, T. K. Lee, I. W. Choi, H. W. Choi, Y. Jo, Y. J. Yoon, J. W. Kim, J. Lee, D. Huh, *Joule* **2019**, *3*, P2179.

[3] E. H. Jung, N. J. Jeon, E. Y. Park, C. S. Moon, T. J. Shin, T.-Y. Yang, J. H. Noh, J. Seo, *Nature* **2019**, *567*, 511.

[4] National Renewable Energy Laboratory, NREL Chart, **2019**, http://www.nrel.gov/ncpv/images/efficiency_chart.jpg (accessed: August 2019).

[5] J. M. Ball, M. M. Lee, A. Hey, H. J. Snaith, *Energy Environ. Sci.* **2013**, *6*, 1739.

[6] S. S. Shin, J. H. Suk, B. J. Kang, W. Yin, S. J. Lee, J. H. Noh, T. K. Ahn, F. Rotermund, I. S. Cho, S. I. Seok, *Energy Environ. Sci.* **2019**, *12*, 958.

[7] J. J. Yoo, S. Wieghold, M. C. Sponseller, M. R. Chua, S. N. Bertram, N. T. P. Hartono, J. S. Tresback, E. C. Hansen, J.-P. Correa-Baena, V. Bulović, T. Buonassisi, S. S. Shin, M. G. Bawendi, *Energy Environ. Sci.* **2019**, *12*, 2192.

[8] S. Bai, P. Da, C. Li, Z. Wang, Z. Yuan, F. Fu, M. Kawecki, X. Liu, N. Sakai, J. T.-W. Wang, S. Huettner, S. Buecheler, M. Fahlman, F. Gao, H. J. Snaith, *Nature* **2019**, *571*, 245.

[9] M. Saliba, T. Matsui, J. Seo, K. Domanski, J. Correa-Baena, M. K. Nazeeruddin, S. Zakeeruddin, W. Tress, A. Abate and A. Hagfeldt, J.-W. Lee, Y. J. Choi, I.-H. Jang, S. Lee, P. J. Yoo, H. Shin, N. Ahn, M. Choi, D. Kim, N.-G. Park, *Nat. Energy* **2016**, *1*, 16081.

[10] T. Singh, T. Miyasaka, *Adv. Energy Mater.* **2018**, *8*, 1700677.

[11] M. Li, C. Zhao, Z. K. Wang, C. C. Zhang, H. K. Lee, A. Pockett, J. Barbé, W. C. Tsoi, Y. G. Yang, M. J. Carnie, *Adv. Energy Mater.* **2018**, *8*, 1801509.

[12] M. Li, Y. G. Yang, Z. K. Wang, T. Kang, Q. Wang, S. H. Turren-Cruz, X. Y. Gao, C. S. Hsu, L. S. Liao, A. Abate, *Adv. Mater.* **2019**, *31*, 1901519.

[13] C. Eames, J. M. Frost, P. R. Barnes, B. C. O'regan, A. Walsh, M. S. Islam, *Nat. Commun.* **2015**, *6*, 7497.

[14] Y. Shao, Y. Fang, T. Li, Q. Wang, Q. Dong, Y. Deng, Y. Yuan, H. Wei, M. Wang, A. Gruverman, *Energy Environ. Sci.* **2016**, *9*, 1752.

[15] C. Li, S. Tscheuschner, F. Paulus, P. E. Hopkinson, J. Kießling, A. Köhler, Y. Vaynzof, S. Huettner, *Adv. Mater.* **2016**, *28*, 2446.

[16] S. Bae, S. Kim, S.-W. Lee, K. J. Cho, S. Park, S. Lee, Y. Kang, H.-S. Lee, D. Kim, *J. Phys. Chem. Lett.* **2016**, *7*, 3091.

[17] Y. Reyna, M. Salado, S. Kazim, A. Pérez-Tomas, S. Ahmad, M. Lira-Cantu, *Nano Energy* **2016**, *30*, 570.

[18] E. L. Unger, E. T. Hoke, C. D. Bailie, W. H. Nguyen, A. R. Bowring, T. Heumüller, M. G. Christoforo, M. D. McGehee, *Energy Environ. Sci.* **2014**, *7*, 3690.

[19] J. Haruyama, K. Sodeyama, L. Han, Y. Tateyama, *J. Am. Chem. Soc.* **2015**, *137*, 10048.

[20] Y. Shao, Z. Xiao, C. Bi, Y. Yuan, J. Huang, *Nat. Commun.* **2014**, *5*, 5784.

[21] D. Wei, F. Ma, R. Wang, S. Dou, P. Cui, H. Huang, J. Ji, E. Jia, X. Jia, S. Sajid, *Adv. Mater.* **2018**, *30*, 1707583.

[22] W. Ke, C. Xiao, C. Wang, B. Saparov, H. S. Duan, D. Zhao, Z. Xiao, P. Schulz, S. P. Harvey, W. Liao, *Adv. Mater.* **2016**, *28*, 5214.

[23] C. E. Halbig, O. Martin, F. Hauke, S. Eigler, A. Hirsch, *Chem. - Eur. J.* **2018**, *24*, 13348.

[24] F. Grote, C. Gruber, F. Börrnert, U. Kaiser, S. Eigler, *Angew. Chem.* **2017**, *129*, 9350.

[25] a) Z. Wang, S. Eigler, Y. Ishii, Y. Hu, C. Papp, O. Lytken, H.-P. Steinrück, M. Halik, *J. Mater. Chem. C* **2015**, *3*, 8595; b) B. Butz, C. Dolle, C. E. Halbig, E. Spiecker, S. Eigler, *Angew. Chem. Int. Ed.* **2016**, *55*, 15771.

[26] H. Chen, Y. Hou, C. E. Halbig, S. Chen, H. Zhang, N. Li, F. Guo, X. Tang, N. Gasparini, I. Levchuk, *J. Mater. Chem. A* **2016**, *4*, 11604.

[27] E. Nouri, Y. L. Wang, Q. Chen, J. J. Xu, G. Paterakis, V. Dracopoulos, Z. X. Xu, D. Tasis, M. R. Mohammadi, P. Lianos, *Electrochim. Acta* **2017**, *233*, 36.

[28] P. Vecera, S. Eigler, M. Koleśnik-Gray, V. Krstić, A. Vierck, J. Maultzsch, R. A. Schäfer, F. Hauke, A. Hirsch, *Sci. Rep.* **2017**, *7*, 45165.

[29] M. Hadadian, J. P. Correa-Baena, E. K. Goharshadi, A. Ummadisingu, J. Y. Seo, J. Luo, S. Gholipour, S. M. Zakeeruddin, M. Saliba, A. Abate, *Adv. Mater.* **2016**, *28*, 8681.

[30] L. L. Jiang, Z. K. Wang, M. Li, C. C. Zhang, Q. Q. Ye, K. H. Hu, D. Z. Lu, P. F. Fang, L. S. Liao, *Adv. Funct. Mater.* **2018**, *28*, 1705875.

[31] M. Li, Z. K. Wang, M. P. Zhuo, Y. Hu, K. H. Hu, Q. Q. Ye, S. M. Jain, Y. G. Yang, X. Y. Gao, L. S. Liao, *Adv. Mater.* **2018**, *30*, 1800258.

[32] M. Xiao, F. Huang, W. Huang, Y. Dkhissi, Y. Zhu, J. Etheridge, A. Gray-Weale, U. Bach, Y. B. Cheng, L. Spiccia, *Angew. Chem., Int. Ed.* **2014**, *53*, 9898.

[33] H. J. Jung, D. Kim, S. Kim, J. Park, V. P. Dravid, B. Shin, *Adv. Mater.* **2018**, *30*, 1802769.

[34] Q. Jeangros, M. Duchamp, J. R. M. Werner, M. Kruth, R. E. Dunin-Borkowski, B. Niesen, C. Ballif, A. Hessler-Wyser, *Nano Lett.* **2016**, *16*, 7013.

[35] J. Li, T. Jiu, S. Chen, L. Liu, Q. Yao, F. Bi, C. Zhao, Z. Wang, M. Zhao, G. Zhang, *Nano Lett.* **2018**, *18*, 6941.

[36] W. Nie, H. Tsai, R. Asadpour, J.-C. Blancon, A. J. Neukirch, G. Gupta, J. J. Crochet, M. Chhowalla, S. Tretiak, M. A. Alam, *Science* **2015**, *347*, 522.

[37] J. P. Correa-Baena, M. Anaya, G. Lozano, W. Tress, K. Domanski, M. Saliba, T. Matsui, T. J. Jacobsson, M. E. Calvo, A. Abate, *Adv. Mater.* **2016**, *28*, 5031.

[38] L. L. Jiang, Z. K. Wang, M. Li, C. H. Li, P. F. Fang, L. S. Liao, *Sol. RRL* **2018**, *2*, 1800149.

[39] A. Pockett, G. E. Eperon, T. Peltola, H. J. Snaith, A. Walker, L. M. Peter, P. J. Cameron, *J. Phys. Chem. C* **2015**, *119*, 3456.

[40] K. Domanski, B. Roose, T. Matsui, M. Saliba, S.-H. Turren-Cruz, J.-P. Correa-Baena, C. R. Carmona, G. Richardson, J. M. Foster, F. De Angelis, *Energy Environ. Sci.* **2017**, *10*, 604.

[41] M. Li, Z. K. Wang, Y. G. Yang, Y. Hu, S. L. Feng, J. M. Wang, X. Y. Gao, L. S. Liao, *Adv. Energy Mater.* **2016**, *6*, 1601156.

[42] M. Li, Z.-K. Wang, T. Kang, Y. Yang, X. Gao, C.-S. Hsu, Y. Li, L.-S. Liao, *Nano Energy* **2018**, *43*, 47.